In$_2$S$_3$ nanomaterial as a broadband spectrum photocatalyst to display significant activity

Wenwen Gao [a], Wenxia Liu [a,*], Yanhua Leng [b], Xiaowei Wang [a], Xingqi Wang [a], Bin Hu [a], Dehai Yu [a], Yuanhua Sang [b], Hong Liu [b,**]

[a] Key Laboratory of Pulp & Paper Science and Technology (Ministry of Education), Qilu University of Technology, Jinan, Shandong 250353, China
[b] State Key Laboratory of Crystal Materials, Shandong University, Jinan, Shandong 250100, China

ARTICLE INFO

ABSTRACT

We, herein, report the synthesis of the first photocatalyst, tetragonal In$_2$S$_3$ nanoparticles, to display broad-spectrum photocatalytic properties under ultraviolet (UV), visible, and near-infrared irradiation from a simple hydrothermal method. The as-synthesized In$_2$S$_3$ nanoparticles have irregular morphology and possess a primary particle size of 5–20 nm with high photo-degradation abilities under UV (96.2% within 30 min), visible light (95.4% within 3 h) and near-infrared light (67.2% within 3 h), a phenomenon extremely rare in character with respect to a broad class of photocatalysts that have a single crystalline phase. This current work in broadband spectrum photocatalysis affords a new paradigm for the full utilization of solar light.

1. Introduction

Due to growing threats of environment pollution and energy shortages, research has campaigned for developing solar-active photocatalysts to address pollution control and energy storage over the past decade [1–8]. Nevertheless, the excitation sources of photocatalysts that have been detected so far have been mostly confined in the spectrum from UV to visible wavelength, whereas near-infrared light accounting for 44% of the incoming solar energy has rarely been utilized because its low photo-energy cannot directly induce the activity of most semiconductors during the process of solar energy conversion [9]. Some pioneering research has been carried out to utilize the near-infrared (NIR) light component (using a 980 nm laser) through combining semiconductors with up-conversion materials, such as rare earth doped YF$_3$, NaYF$_4$, CaF$_2$ [10–14], to form heterojunctions, in which the NIR light was absorbed by up-conversion materials and switched to visible or UV light. The visible or UV light excites the semiconductor photocatalysts to induce photocatalytic reactions [15–17]. The photocatalytic activity of those up-conversion-based photocatalysts is significantly dependent on the properties of the up-conversion materials and light absorption of the semiconductors. Although improved up-conversion materials such as β-NaYF$_4$:Yb^{3+}, Tm^{3+} with larger microcrystals, which are known to have much higher up-conversion efficiency than their nano-counterparts, have been employed to constitute core–shell structures with semiconductors to increase both the up-conversion efficiency and the light absorption, these types of materials still show rather low photocatalytic efficiencies on degradation of organic pollutants due to their weak infrared (IR) absorption [18]. The IR absorption is probably further weakened by the shielding light effect between the up-conversion materials and the semiconductors, and the low NIR to UV up-conversion efficiency [19]. Furthermore, a tedious preparation process, coming at high cost and less than desirable environmental impact (use of rare earth elements), as well as the application of a 980 nm laser as the near-infrared source restricts the implementation of this strategy. Using carbon-dots (CDs), which exhibit a large cross section of up-conversion absorption and emission (to match semiconductors such as Cu$_2$O), provide a possibility of expanding NIR absorption range and improving the degradation efficiency [20]. However, directly utilizing NIR energy to decompose organic contaminants is still a nearly non-existent research topic and a very challenging task. Of the few infrared light active photocatalysts, Cu$_2$(OH)PO$_4$, in which axially elongated CuO$_4$(OH)$_2$ octahedra share their corners with axially compressed CuO$_4$(OH) trigonal bipyramids, has been able to oxidize 2,4-dichlorophenol in aqueous solution by Cu^{III} sites at the CuO$_4$(OH) trigonal

* Corresponding author at: Key Laboratory of Pulp & Paper Science and Technology (Ministry of Education), Qilu University of Technology, Daxue Road, Western University Science Park, Jinan, Shandong 250353, China. Tel.: +86 531 89631168; fax: +86 531 88574135.
** Corresponding author.
E-mail addresses: liuwenxia@qlu.edu.cn (W. Liu), hongliu@sdu.edu.cn (H. Liu).

bipyramids originating from transferring photogenerated electrons to the neighboring $CuO_4(OH)_2$ octahedra under NIR irradiation. Thus, it acts more like a redox catalyst activated by NIR energy [21]. TiO_2-supported $Ce(III)_2Ti_2O_7$, produced by the aqueous hydrolysis of a cerium-containing polyoxotitanium cages, exhibits broad-band absorption behavior as a result of the combined effects of lowering the band gap, extending the absorption into the visible region, and potential up-conversion. Regrettably, its photoactivity under NIR radiation is very low [22]. Bi_2WO_6 nanosheets with an orthorhombic structure and a growth direction of (0 0 1) plane possess good NIR photocatalytic degradation of methyl orange (MO) due to the oxygen vacancies of the Bi_2WO_6. The oxygen vacancies can raise the Fermi level and reduce the band edge, allowing interband transitions and carrier creation under NIR illumination. Nevertheless, the UV photocatalytic degradation effect of the Bi_2WO_6 nanosheets toward MO is rather low. To truly realize efficient broad spectrum photocatalytic degradation of MO, the Bi_2WO_6 nanosheets must be combined with other UV photocatalysts such as TiO_2 nanobelts [23]. In consideration of the above practical limitations of such techniques for application in solar energy schemes, it is desirable to develop alternative photocatalysts that can be activated effectively by broadband spectrum irradiation.

Among various photocatalysts that have been reported, indium sulfide (In_2S_3) has attracted special interest and been considered as a promising candidate for optoelectronic and photovoltaic applications due to its low toxicity, high carrier mobility, and stability at ambient conditions [24]. In_2S_3 exhibits three different structural forms: α-In_2S_3, β-In_2S_3, and γ-In_2S_3. Among these crystalline structures, β-In_2S_3, the most stable structural form, has been extensively investigated as an excellent visible light-driven photocatalyst and sensitizer for wide band-gap semiconductor photocatalysts [25–27]. More importantly, due to the defect spinel structure of β-In_2S_3, it can allow the existence of intrinsic vacant sites. Such an interesting defect structure of β-In_2S_3 is especially helpful to realize any possible NIR-driven photocatalysis because these vacancies display electron affinity and can act as electron traps [28]. However, to the best of our knowledge, no related report on near-infrared photocatalysis activity of In_2S_3 has been published, although, it has been extensively studied as a visible light photocatalyst.

Herein, we set about synthesizing In_2S_3 nanoparticles via a simple hydrothermal reaction of indium nitrate with sodium sulfide and performing photocatalysis experiments of the as-synthesized In_2S_3 for degradation of MO under a wide spectrum of solar energies, including NIR. It is discovered that the as-synthesized In_2S_3 possesses excellent UV, visible and NIR photocatalytic activities. Even more intriguing, the photocatalytic performance of the as-synthesized In_2S_3 nanoparticles is very stable under irradiation in the UV–vis–NIR region. This is the first photocatalyst to our knowledge with high photocatalytic activity over the entire solar light spectrum. Such a discovery will promote the development of new photocatalysts that are active over the full electromagnetic spectrum, and open the door to practical utilization of solar energy.

2. Experimental

2.1. Materials

Sodium hydroxide (NaOH), nitric acid (HNO_3), sodium sulfide ($Na_2S·9H_2O$), indium nitrate ($In(NO_3)_3·4.5H_2O$) and methyl orange (MO) were supplied by Sinopharm Chemical Reagents Co., Ltd. Terephthalic acid (TA) was analytical grade and purchased from Aladdin Industrial Corporation. Titania P25 (TiO_2, ca. 80% anatase and 20% rutile) was commercial TiO_2 powder from Evonik Degussa GmbH. According to the supplier's report, the P25 has an

average primary particle size of 21 nm and a specific surface area of $50 ± 15 \ m^2/g$. All other reagents were analytical grade and used directly without further purification. Deionized water was used throughout this study.

2.2. Synthesis of In_2S_3 nanoparticles

In_2S_3 nanoparticles were synthesized through a hydrothermal procedure. 0.48 mmol $In(NO_3)_3·4.5H_2O$ and 1.2 mmol $Na_2S·9H_2O$ were, respectively, dissolved in 40 ml deionized water at room temperature. After fully dissolved, the prepared sodium sulfide aqueous solution was gradually added to the indium nitrate solution under agitation to obtain a homogeneous pale yellow sol. The sol was neutralized to a pH lower than 3.0 by adding dilute nitric acid, and transferred into a 100 ml Teflon-lined autoclave, followed by a hydrothermal treatment at 180 °C for 24 h. When the autoclave cooled to room temperature, the as-synthesized orange precipitate was collected, washed sequentially with deionized water and alcohol several times, and dried in a vacuum oven at 55 °C for 12 h.

2.3. Characterization

The morphologies and size of the as-synthesized In_2S_3 nanoparticles were characterized with a HITACHI S-4800 field-emission scanning electron microscope (FE-SEM). Energy-dispersive X-ray (EDX) spectrometer coupled to the FE-SEM was used to analyze the chemical composition of In_2S_3 powder. X-ray diffraction (XRD) pattern of the In_2S_3 nanoparticles was recorded on a Bruke D8 Advance powder X-ray diffractometer with Cu Kα radiation ($\lambda = 0.15406$ nm). The N_2 adsorption–desorption isotherms of the nanoparticles were measured using a Micromeritics TriStar 3020 instrument. Specific surface area was calculated by the Brunauer–Emmett–Teller (BET) technique from an N_2 adsorption isotherm, and the pore size distribution was determined by desorption isotherm using the Barrett–Joiner–Halenda (BJH) method. To further investigate the structure details of the as-synthesized nanoparticles, high-resolution transmission electron microscopy (HRTEM) was employed, and the images were obtained with a JEOL JEM 2100 microscope. The UV–vis diffuse reflectance absorption spectrum (DRS) of the sample was collected on a UV–vis spectrophotometer (UV-2550, Shimadzu) with an integrating sphere attachment, while the analytic range was 300–800 nm. The vis–NIR DRS of the sample was recorded on a UV–vis–NIR spectrophotometer (Cary 5000, Varian) with an integrating sphere attachment in the range of 600–2400 nm. In both UV–vis and UV–vis–NIR DRS, $BaSO_4$ was used as the reflectance standard. The surface elemental composition and valence state of the sample was detected by X-ray photoelectron spectra (XPS), which were recorded on an ESCALAB 250 photoelectron spectrometer. All of the binding energies were calibrated by the C1s peak at 284.6 eV. The Fourier-transform infrared (FTIR) spectra of the samples were obtained on a Nicolet Avatar 370 infrared spectrometer in the range of 400–4000 cm^{-1} using pressed KBr discs. Photoelectrochemical analyses were carried out on an electrochemical workstation (Gamry Reference 600, USA) with a standard three-electrode cell by using Ag/AgCl as reference electrode and Pt wire as the counter electrode, respectively, in 1 M H_2SO_4 solution. The working electrodes were prepared by depositing the sample slurries onto a clean fluorine doped tin oxide (FTO) glass surface [29,30], followed by a 2 h calcination at 500 °C with flowing N_2 to form a better electronic connection between the sample and the FTO substrate. To eliminate the effect of the anode on the PEC response, the In_2S_3 anode was subjected to cyclic voltammetry (CV) over 9 cycles in a 1 M H_2SO_4 electrolyte before stable signals were recorded. Then the dark current and the photocurrent of the In_2S_3 anode under NIR light irradiation

were recorded with voltage bias ranging from -0.4 V to 0.1 V. The photocurrent response curves were recorded under NIR light irradiation with light on–off switches of 500 s at a bias of -0.3 V. The blank anode was obtained from the anode by removing the In_2S_3 nanoparticles off the FTO glass. The production of hydroxyl radicals ($\bullet$OH) on the surface of In_2S_3 nanoparticles under NIR light irradiation was detected by the photoluminescence (PL) technique using terephthalic acid (TA) as a probe molecule [31,32]. Aqueous mixture of In_2S_3 nanoparticles and TA was prepared by adding 20 mg of In_2S_3 nanoparticles into 20 mL of TA/NaOH aqueous solution, in which the concentrations of TA and NaOH were 83 mg L^{-1} and 80 mg L^{-1}, respectively. After the aqueous mixture was illuminated for some time under NIR light, which was provided by a 250 W infrared lamp with a cut-off filter (<720 nm) [23], the nanoparticles were removed from the mixture by centrifuging at 10,000 revolutions per minute (rpm) for 5 min. The PL spectrum of supernatant was recorded on an F-4600 FL spectrophotometer with an excitation wavelength of 315 nm.

2.4. Photocatalytic activity test

The photocatalysis of In_2S_3 nanoparticles was evaluated by their ability to degrade methyl orange (MO) from an aqueous solution under lighting. In a typical experiment, 20 mg of photocatalyst was added into a 50 ml quartz test tube containing 20 mL of MO aqueous solution with a concentration of 20 mg L^{-1}. Prior to illumination, the suspension was magnetically stirred in a dark condition for 30 min to achieve a homogenous dispersion and reach adsorption–desorption equilibrium between the dye and the catalyst surface under ambient conditions. In details, a 500 W mercury lamp with a primary wavelength of 365 nm and a 350 W Xe arc lamp equipped with an UV optical filter for cutting off the light of wavelength below 380 nm were chosen as the UV and visible irradiation sources, respectively. A 150 W APOLLO solar simulator (Newport

94,022A) was used as a simulated solar light source. During NIR photodegradation process, a 250 W infrared lamp with a cut-off filter ($\lambda < 720$ nm) was used as NIR light resource based on the report of Tian et al. [23].

In these photoreaction experiments, the activity tests of In_2S_3 under UV and visible irradiation were carried out in the same photocatalytic reactor system in which the highest temperature was kept at 25 °C by circling cool water. In comparison with this, it was rather difficult to control the temperature below 25 °C under NIR irradiation because water continued to absorb and convert electromagnetic radiation into heat. In the NIR photoreaction, ice bags were, thus, chosen to slow down the sharp increase in the temperature of suspension over an extended period (Fig. 4b). At various irradiation time intervals, an aliquot of the mixed solution was collected, immediately centrifuged at 10,000 revolutions per minute (rpm) for 5 min to separate the catalyst particles from the mixed liquid. The UV–vis absorption intensity of MO supernatant was measured directly via UV–vis spectrophotometer (Hitachi UV-300) at 465 nm where the degradation rate could be monitored.

3. Results and discussion

3.1. Crystal structure and morphology

The as-synthesized In_2S_3 sample is an orange powder (inset of Fig. 1a). The crystalline phase and morphology of the as-synthesized In_2S_3 sample were characterized by X-ray diffraction (XRD) and scanning electron microscopy (SEM). N_2 adsorption–desorption isotherm was used to detect the microspores and specific surface area of the sample. The XRD peaks of the as-synthesized sample, shown in Fig. 1a, can be indexed to β-In_2S_3 tetragonal phase by careful comparison with JCPDS card file no. 25-0390. No XRD peak arising from the possible impurities, such as In_2O_3 or InS, is detected, indicating its high purity. The
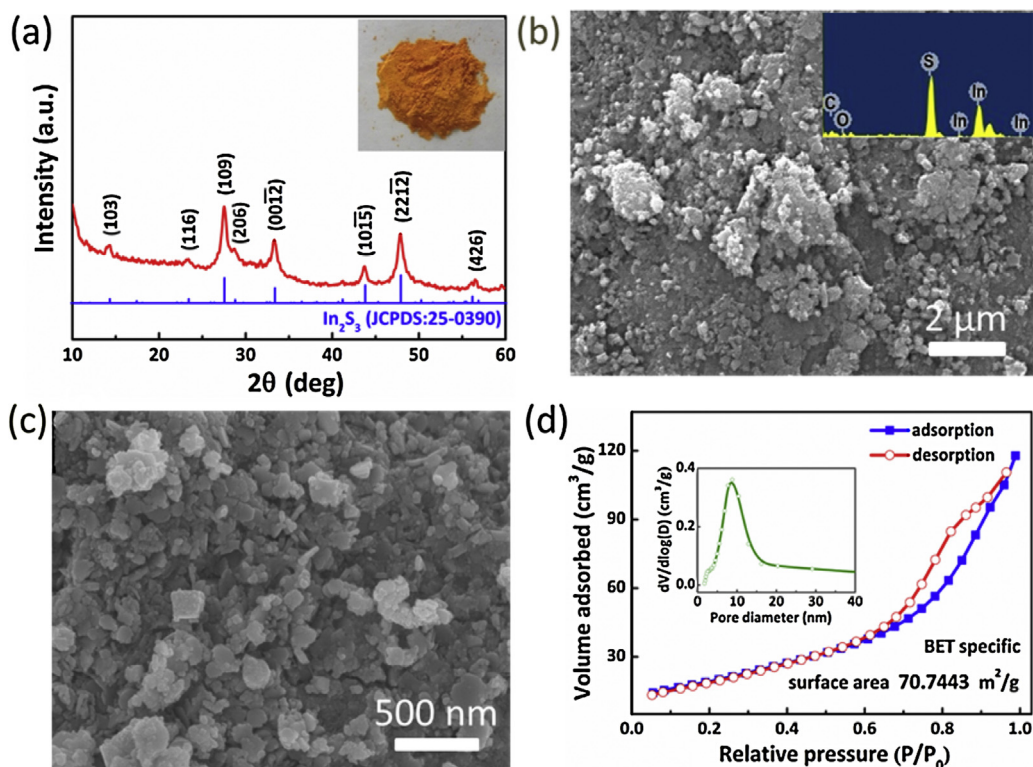

Fig. 1. (a) XRD pattern, inset is the photograph of as-synthesized In_2S_3 nanoparticles; (b and c) SEM images, inset shown in plane b is EDX analysis; (d) N_2 adsorption–desorption isotherm of In_2S_3, inset is corresponding pore size distribution curve.
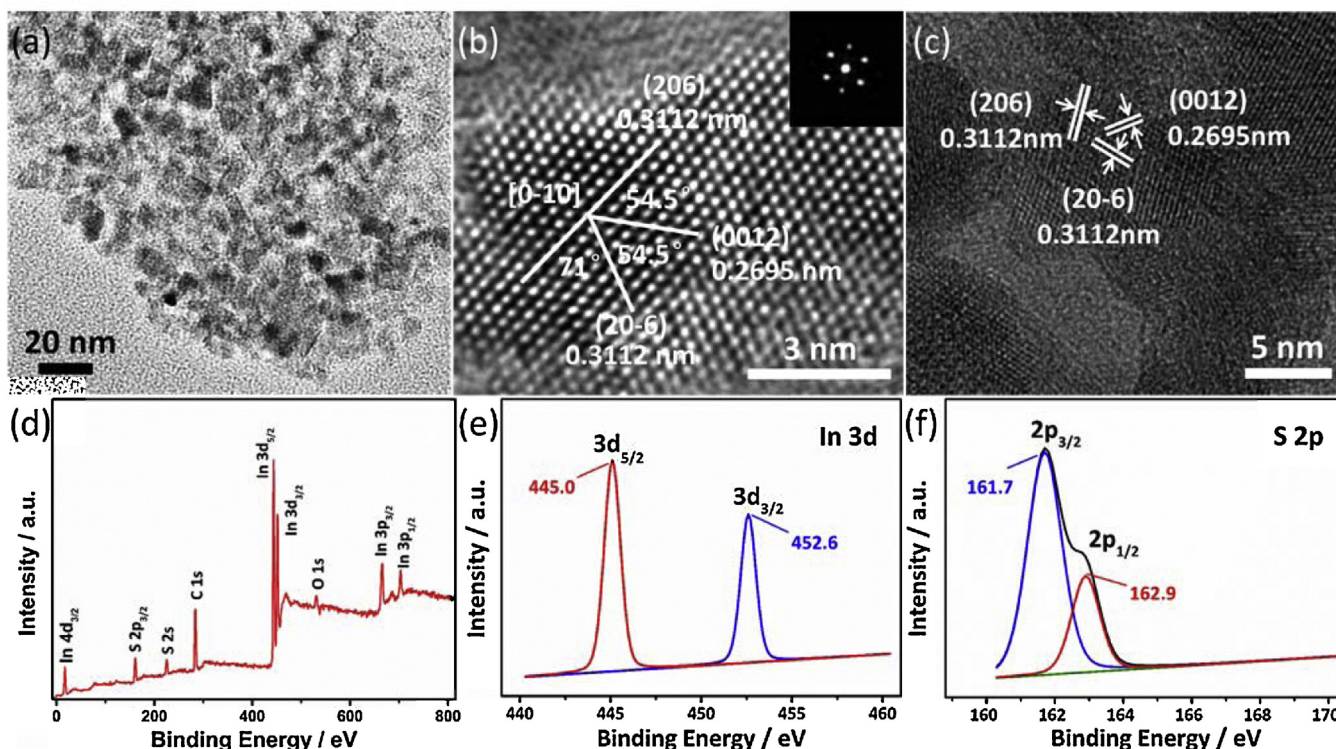
Fig. 2. (a) TEM image, (b and c) HRTEM images of In_2S_3 nanoparticles, inset shown in plan b is the Fourier transform electron diffraction pattern of In_2S_3; (d) XPS fully scanned spectrum, (e) In_{3d} and (f) S_{2p} core-level XPS spectra of In_2S_3.

reflection peaks are considerably sharp, indicating that the product is well crystallized.

In the typical SEM image of the as-synthesized In_2S_3 sample shown in Fig. 1b, some micro-sized chunks are observed. From the high-resolution SEM image of the In_2S_3 powder, shown in Fig. 1c, it can be found that the micro-chunks are formed by the aggregation of large amounts of nanoparticles. The In_2S_3 nanoparticles are granular in morphology, and have a primary particle size less than 20 nm. Energy dispersive X-ray (EDX) spectrum (inset of Fig. 1b) demonstrates that the as-synthesized product predominantly consists of sulfur and indium. The specific surface area, which was calculated by BET method from N_2 adsorption isotherm (Fig. 1d), of the aggregated sample is as large as $70.74 \, m^2/g$ due to its small primary particle size. According to the pore distribution curve (inset of Fig. 1d), the aggregated In_2S_3 sample possesses mesopores with diameters uniformly at 8.8 nm, which is in the same order with respect to the size of its primary particles, corroborating the granular shape and aggregation character of the as-synthesized sample.

3.2. Microstructure and chemical states

The microstructure of In_2S_3 nanoparticles were further investigated with high-resolution transmission electron microscopy (HRTEM). The HRTEM image, shown in Fig. 2a, further confirms that most of the In_2S_3 nanoparticles have irregular shapes. The primary particles with a particle size of 5–20 nm were gradually formed during the hydrothermal treatment at $180\,°C$ for 24 h. However, some cuboid-shaped nanocrystals can also be found. By measuring the lattice fringes in Fig. 2b and c, the resolved interplanar distances are found to be 0.311, 0.269 nm, corresponding to the planes (2 0 6), (0 0 12) of tetragonal In_2S_3. As discussed above, the as-synthesized In_2S_3 nanoparticles are well crystallized, and have very small particle sizes, which match the essential characteristics

of high performance nanostructured photocatalysts. The synthesis of high crystalline cuboid In_2S_3 is attributed to the modified two-step synthesis route and utilization of $In(NO_3)_3$ as the indium source during the co-precipitation process.

The surface chemical composition and valence states of the as-prepared In_2S_3 nanoparticles were investigated by X-ray photoelectron spectrometry (XPS) measurements. The fully scanned spectrum of In_2S_3 sample is shown in Fig. 2d, which reveals the presence of elements In, S, O and C. The observed C peak at 284.6 eV may be ascribed to an adventitious carbon-based contaminant, which is used to calibrate all of the binding energies, while the O element is due to the absorption of oxygen or carbon dioxide on the surface of the In_2S_3 nanoparticles because of their exposure to the atmosphere. The XPS spectrum of the In_2S_3 sample is similar and consistent with the typical In_2S_3 spectrum reported in the literature [33]. High-resolution spectra of In_{3d} and S_{2p} are shown in Fig. 2e and f, respectively. The XPS spectrum of In_{3d} possesses two symmetrical peaks at the binding energies of 445.0 eV for In $3d_{5/2}$ and 452.6 eV for In $3d_{3/2}$, while the two strong peaks at 161.7 and 162.9 eV in the S_{2p} spectrum are attributed to the binding energy of $S_{2p3/2}$ and $S_{2p1/2}$, respectively. These values are in good agreement with the reported data [30]. The peak separations of In_{3d} and S_{2p} are calculated to be 7.6 eV and 1.2 eV, and the two peak area ratios of $In_{3d3/2}$–$In_{3d5/2}$ and $S_{2p1/2}$–$S_{2p3/2}$ are ca. 2:3 and 1:2.8, respectively. These results indicate that the In and S are present as In^{3+} and S^{2-} [34]. However, the atomic ratio of sulfur to indium was calculated to be 1.22, which is smaller than the theoretical value of 1.5, suggesting either the existence of sulfur vacancies or oxidation in the as-synthesized In_2S_3 nanoparticle surfaces.

3.3. Photocatalytic activity

To evaluate the photocatalytic activity of photocatalysts, methyl orange (MO), a very stable azo dye, was used as a model
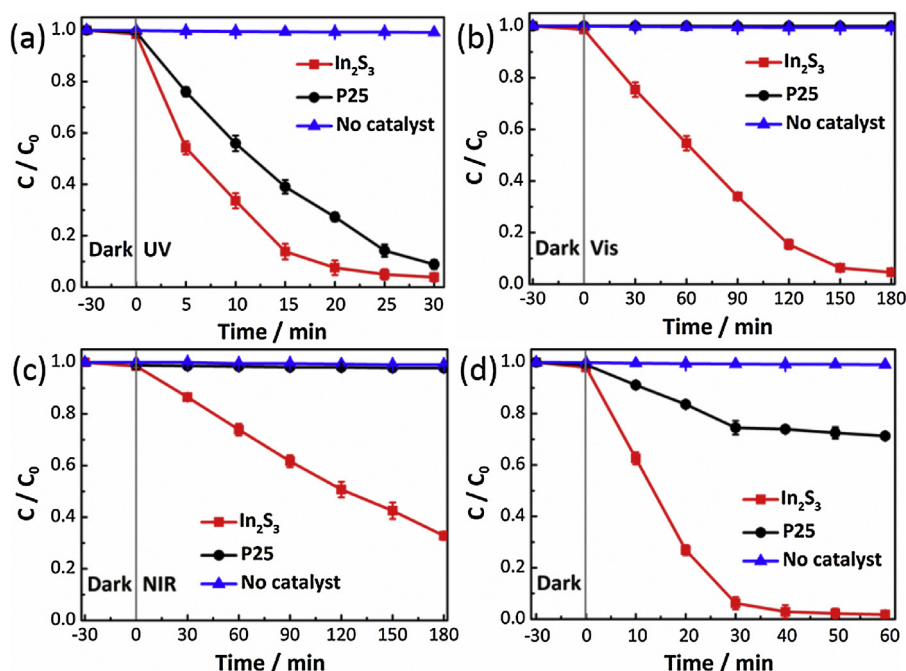
Fig. 3. Photocatalytic degradation of MO in the presence of P25, In_2S_3 nanoparticles and without any catalyst for comparison tests under (a) UV light, (b) visible light, (c) near-infrared light and (d) simulated sunlight irradiation.

pollutant [35]. Fig. 3a–d, respectively, reveal the degradation of MO by In_2S_3 nanoparticles under UV, visible, NIR, and simulated solar light irradiation as a function of irradiation time. Ahead of light irradiation, the aqueous mixture of MO and In_2S_3 was maintained for 30 min under stirring in the dark to reach an adsorption–desorption equilibrium. For comparison, the self-degradation of MO and its decomposition catalyzed by commercial P25 were also measured under the same experimental conditions. The degradation rate of MO was calculated by $(1-C/C_0) \times 100\%$, where C is the concentration of MO at the irradiation time t and C_0 is the original concentration before adsorption equilibrium. The results show that the concentration of dye shows hardly any decrease when the MO was irradiated alone under UV, visible, NIR, and simulated solar light over a given time, which confirms that the decoloration of
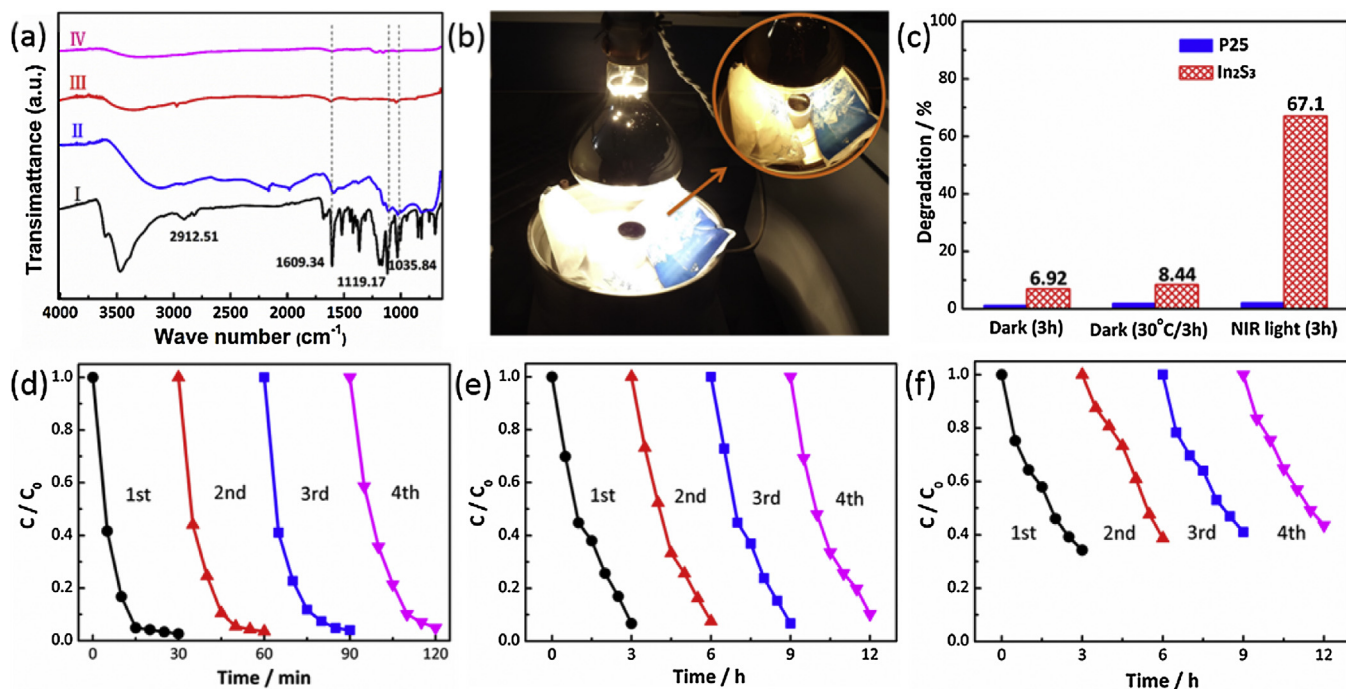

Fig. 4. (a) FTIR spectra of (I) methyl orange, (II) In_2S_3 nanoparticles after mixing with MO aqueous solution in the dark for 3 h at 30 °C, (III) In_2S_3 nanoparticles after mixing with MO aqueous solution in the dark for 3 h followed by irradiating under near-infrared light for 8 h, (IV) pristine In_2S_3 nanoparticles; (b) photograph of the experimental device used for NIR photoreaction; (c) photocatalytic degradation of MO in the presence of P25, In_2S_3 nanoparticles at ambient conditions, 30 °C in the dark, and under near-infrared light irradiation for 3 h, irradiation-time dependence of photocatalytic degradation of MO aqueous solution over In_2S_3 nanoparticles during repeated photooxidation experiments under; (d) UV light; (e) visible light and (f) near-infrared light irradiation.

dye in the presence of photocatalysts results from the photocatalysis. Meanwhile, both the In_2S_3 and P25 samples show very low adsorption capacities of MO. The decoloration of MO, therefore, is attributed to the photocatalytic degradation.

Fig. 3a and b shows UV and visible light-driven photocatalytic activity of the above samples on the degradation of MO. From Fig. 3a, the UV photocatalytic activity of In_2S_3 sample is even much higher than that of P25. After 30 min UV-light irradiation, 96.2% of MO was photodegraded by the In_2S_3 sample, whereas only 91.2% by P25 nanoparticles. As is well known, the high UV photocatalytic activity of P25 is attributed to the co-existence of two crystalline phases, anatase and rutile, in one granular particle, which benefits separation of the photo-induced carriers [36]. However, for the In_2S_3 nanoparticles in this work, the product powder has only a single crystalline phase. Its high photocatalytic activity must, therefore, be attributed to its defect spinel structure, in which the vacancies act as electron traps to prevent the recombination of the photo-induced carriers [28]. Similar to the results from previous work [37], MO degradation demonstrates that P25 hardly exhibits visible photocatalytic degradation while the In_2S_3 nanoparticles demonstrate highly exemplary visible photocatalytic activities, as shown in Fig. 3b. After 3 h of visible-light irradiation, the degradation rate of MO catalyzed by P25 is negligible, while that catalyzed by the In_2S_3 increases to nearly 95.4%.

Most excitingly, the In_2S_3 nanoparticles are detected to possess a rather high NIR light photocatalytic activity, whereas it has been previously reported to be a visible-light driven photocatalyst. As indicated in Fig. 3c, the corresponding MO degradation rate under 3 h NIR light irradiation for In_2S_3 is 67.2%, which is in sharp contrast with the negligible MO degradation value for P25. In longer trials, up to 8 h, approximately 97% of the dye could be decolorized under NIR light exposure.

Even more satisfactorily, In_2S_3 nanoparticles demonstrate highly exemplary photocatalytic activity under the irradiation of simulated sunlight. As shown in Fig. 3d, the MO degradation rate for In_2S_3 nanoparticles increases to nearly 100% after 40 min simulated sunlight irradiation. In contrast, the corresponding MO degradation rate for P25 is only 28.7% after 60 min simulated sunlight

irradiation. This indicates that the In_2S_3 nanoparticles are competent solar light-driven photocatalyst.

The decomposition of MO under NIR light could be identified by analysing the FT-IR spectra of In_2S_3–MO mixture before and after NIR light irradiation. Fig. 4a shows the FTIR spectra of methyl orange (curve I), In_2S_3 nanoparticles after mixing with MO aqueous solution ($20\,mg\,L^{-1}$) in the dark for 3 h at $30\,°C$ (curve II), In_2S_3 nanoparticles after mixing with MO aqueous solution ($20\,mg\,L^{-1}$) in the dark for 3 h followed by irradiating under NIR light for 8 h (curve III) and pristine In_2S_3 nanoparticles (curve IV).

As shown in Fig. 4a, the FTIR spectrum of MO (curveI) displays peaks corresponding to the asymmetric $-CH_3$ stretching vibrations at $2912.51\,cm^{-1}$, ring vibrations at $1035.84\,cm^{-1}$, and the aromatic $-C=C-$ ring stretching vibration at $1609.34\,cm^{-1}$. The peak at $1419.61\,cm^{-1}$ is assigned to $-N=N-$ stretching vibration. The peak at $1367.5\,cm^{-1}$ is for the C—N stretching vibration that the N is connected to aromatic ring, while peaks at $1119.17\,cm^{-1}$ and $1039\,cm^{-1}$ come from the vibration of sulfonic group. This confirms the aromatic, azo and sulfonic nature of the dye. In the IR spectrum of In_2S_3 after interacting with $20\,mg\,L^{-1}$ MO in the dark at $30\,°C$ for 3 h, as shown in curve II, weak adsorption peaks at $1035.84\,cm^{-1}$, $1609.34\,cm^{-1}$ and $1119.17\,cm^{-1}$ reveal the weak adsorption of MO. Nevertheless, with the NIR illumination for 8 h, no peaks corresponding to MO can be observed in curve III except for the peaks similar to that of In_2S_3 powders as shown in curve IV, which suggests a complete NIR light degradation of MO process.

Considering the sharp increase in water temperature due to the intense absorption of water on electromagnetic radiation in the infrared region [38], as shown in Fig. 4b, ice bags were chosen to control the temperature of reaction solution under NIR irradiation. However, it was rather difficult to control the temperature below $25\,°C$, as in the case of UV and visible light irradiations, the temperature was then kept below $30\,°C$ to reduce the possibility of any possible contributions from thermal degradation. Meanwhile, thermocatalytic reference experiment at $30\,°C$ in the dark was carried out, the results were shown in Fig. 4c. It can be found from Fig. 4c that when the reaction sample kept at $30\,°C$ in dark for 3 h, the degradation rate of MO is only 8.44%, which is much less than
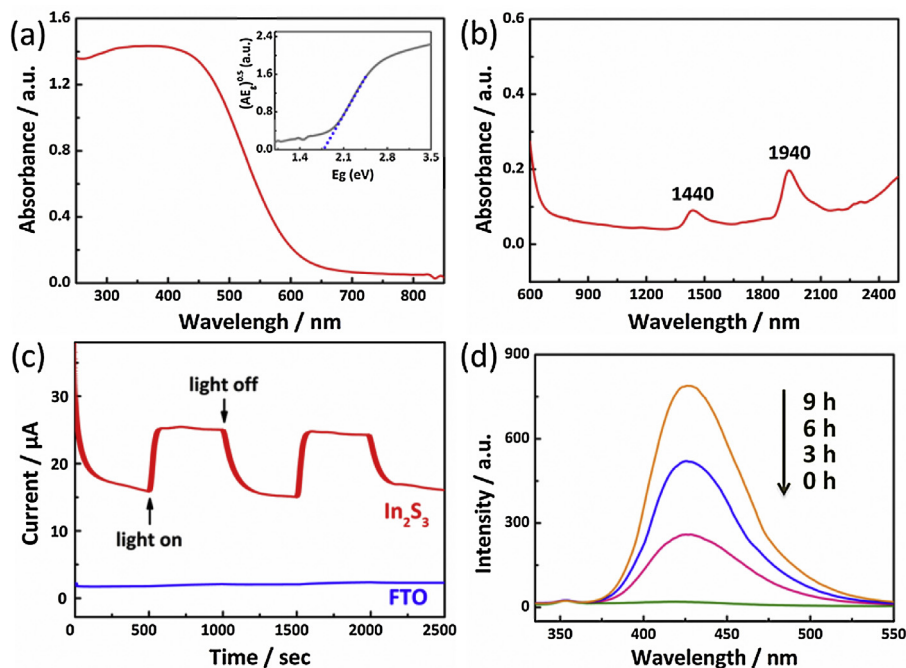

Fig. 5. (a) UV–vis diffuse reflectance absorption (DRS) spectrum; (b) vis–NIR DRS spectrum of pure In_2S_3 nanoparticles; (c) photocurrent generation on In_2S_3 nanoparticles under near-infrared light; (d) •OH-trapping PL spectra of In_2S_3/TA solution under near-infrared light.

the degradation rate of 67.2% obtained under the exposure of NIR light at the same time. Based on the above results, it can be concluded that the NIR photocatalytic activity of In_2S_3 is attributed to photocatalysis instead of a NIR light-induced temperature effect.

To investigate the stability of the In_2S_3 nanoparticles under UV, visible and NIR light irradiation, the same samples were recycled for four times after separation via centrifugation, and the results are shown in Fig. 3g–i. Amazingly, after the excitation of UV, visible and NIR lights, the degradation rate of MO is only reduced, respectively, by 2.3%, 3.8% and 14.1%, after four repeated trials. That is to say, In_2S_3 displays very stable photocatalytic activity over a full-spectrum solar light.

3.4. Optical properties and detection of hydroxyl radicals

To explore the origin of the high photocatalytic activity of In_2S_3 nanoparticles, particularly in the NIR region, additional experiments were needed. UV–vis diffuse reflectance absorption spectrum (DRS) over a wavelength range between 200 and 1000 nm was recorded to explain the UV–vis light photocatalytic property of In_2S_3. As shown in Fig. 5a, the In_2S_3 nanoparticles show significant absorption up to the visible range of over 650 nm, which almost covers the entire visible region. The very broad light absorption region is the main reason for its high UV–vis-light photocatalytic activity. The corresponding band gap energy is estimated to be 1.77 eV (insert in Fig. 5a), which is a little narrower than the value reported previously [26,35]. Furthermore, the steep absorption edge is an evidence of a narrow size distribution and uniform crystallites of In_2S_3 nanoparticles [39], which have been confirmed by TEM (Fig. 2a).

Visible and NIR absorption spectra were recorded to support the NIR light photocatalytic activity of In_2S_3 nanoparticles. In the NIR light region, the In_2S_3 nanoparticles show absorption and display two obvious broad absorption peaks at 1440 nm and 1940 nm (Fig. 5b), which can be ascribed to the presence of a defect band located above the valence band of β-In_2S_3 as reported by Jayakrishnan et al. [40]. The good NIR photocatalytic performance of the In_2S_3 nanoparticles can be attributed to the absorption of NIR light.

Fig. 5c displays the transient photocurrent response of In_2S_3 anode recorded under NIR light irradiation with on–off switches of 500 s. Under illumination, the photocurrent response is as high as 10.5 μA. By contrast, no significant current is observed in the dark for In_2S_3 sample. The photocurrent is formed mainly by diffusion of the photogenerated electrons to the back contact; while, the photoinduced holes are subsumed by the hole acceptor in the electrolyte [35]. The In_2S_3 electrode demonstrated a rapid NIR light photocurrent response, indicating efficient separation and a longer lifetime of photogenerated charge carriers under NIR light irradiation.

The efficient carrier separation of the In_2S_3 nanoparticles can be attributed to the defect spinal structure of β-In_2S_3 and the presence of sulfur vacancies or oxygen in the as-synthesized In_2S_3 nanoparticle surfaces. It is well known that both octahedral and tetrahedral sites in the defect spinel structure of In_2S_3 are occupied by Indium. However, only two-thirds of the tetrahedral sites are filled by indium and the other one-third is empty in order to maintain the stoichiometry of In_2S_3, resulting in a large amount of cation-vacancies in ordered In_2S_3 crystals. These vacancies exhibit electron affinity and can act as electron traps [28], promoting the separation of photogenerated charge carriers under NIR light irradiation. Meanwhile, sulfur vacancies and oxygen in the as-synthesized In_2S_3 nanoparticle surfaces may help to form a defect band above the valence band of In_2S_3 nanoparticles [28]. The defect band not only produces the absorption of NIR light, but also favors the separation of carriers by first trapping the electrons and then slowly releases these electrons into the conductive band [40]. How-

ever, to give a more detailed explanation for the NIR photocatalytic activity of the as-prepared In_2S_3 nanoparticles, their electronic band structure should be explored in the future research.

Hydroxyl radicals are known as a key active specie in the processes of organic pollutant photodegradation [41,42]. At present, the common detection techniques for hydroxyl radicals include high performance liquid chromatography (HPLC), spin-trapping electron paramagnetic resonance (EPR), and chemical fluorometric assay [43]. As a highly sensitive and simple method, terephthalic acid photoluminescence probing technique (TAPL) has been widely used in the detection of hydroxyl radicals [44]. During the photocatalytic process, the TA probes hydroxyl radicals to form 2-hydroxylterephthalic acid (HTA), which exhibits a strong fluorescence peak in 426 nm (λex = 315 nm), so that the hydroxyl radicals can be indirectly detected via measuring the fluorescence of HTA. The PL spectra of In_2S_3/TA solution after NIR light irradiation are shown in Fig. 5d. As shown, the PL emission peak of HTA (λem = 426 nm) is produced by the NIR light illumination, and the intensity of the peak is increased steadily with the irradiation time. This suggests that the hydroxyl radicals are produced under the illumination of NIR light, and the concentration of the hydroxyl radicals is increased steadily with the irradiation time.

All these measurements demonstrate that In_2S_3 nanoparticles prepared via a simple hydrothermal method display a significant broad spectrum especially NIR light photocatalytic activity.

4. Conclusions

An excellent broadband photocatalytic activity for tetragonal In_2S_3 nanoparticles (especially with respect to NIR light irradiation) has been demonstrated. Their excellent photocatalytic properties hence, allow In_2S_3 nanoparticles alone to degrade organic pollutant under the exposure of solar light from the UV to NIR region. This activity of the In_2S_3 product originates from its intrinsically narrow band gap and excellent photoactivity. This discovery is of high significance for full utilization of solar energy, and opens a new door to harnessing full solar light.

Acknowledgements

References

[1] X. Wang, M. Liao, Y. Zhong, J.Y. Zheng, W. Tian, T. Zhai, C. Zhi, Y. Ma, J. Yao, Y. Bando, Adv. Mater. 24 (2012) 3421–3425.
[2] H. Tong, S. Ouyang, Y. Bi, N. Umezawa, M. Oshikiri, J. Ye, Adv. Mater. 24 (2012) 229–251.
[3] C. Yu, G. Li, S. Kumar, K. Yang, R. Jin, Adv. Mater. 26 (2014) 892–898.
[4] W. Guo, F. Zhang, C. Lin, Z.L. Wang, Adv. Mater. 24 (2012) 4761–4764.
[5] I. Justicia, P. Ordejón, G. Canto, J.L. Mozos, J. Fraxedas, G.A. Battiston, R. Gerbasi, A. Figueras, Adv. Mater. 14 (2002) 1399–1402.
[6] Y. Liang, H. Wang, H.S. Casalongue, Z. Chen, H. Dai, Nano. Res. 3 (2010) 701–705.
[7] N. Zhang, M. Yang, X. Tang, Y. Xu, ACS Nano. 8 (2014) 623–633.
[8] M. Yang, B. Zhang, M. Pagliaro, Y. Xu, Chem. Soc. Rev. 43 (2014) 8240–8254.
[9] W. Qin, D. Zhang, D. Zhao, L. Wang, K. Zheng, Chem. Commun. 46 (2010) 2304–2306.
[10] Z. Li, C. Li, Y. Mei, L. Wang, G. Du, Y. Xiong, Nanoscale 5 (2013) 3030–3036.
[11] D. Gao, X. Zhang, W. Gao, ACS Appl. Mater. Inter. 5 (2013) 9732–9739.
[12] S. Huang, N. Zhu, Z. Lou, L. Gu, C. Miao, H. Yuan, A. Shan, Nanoscale 6 (2014) 1362–1364.
[13] J. Zhuang, X. Yang, J. Fu, C. Liang, M. Wu, J. Wang, Q. Su, Cryst. Growth Des. 13 (2013) 2292–2297.
[14] Y. Zhang, Z. Hong, Nanoscale 5 (2013) 8930–8933.

[15] Z. Wang, Y. Liu, B. Huang, Y. Dai, Z. Lou, G. Wang, X. Zhang, X. Qin, Phys. Chem. Chem. Phys. 16 (2014) 2758–2774.
[16] C. Han, M. Yang, B. Wang, Y. Xu, Phys. Chem. Chem. Phys. 16 (2014) 16891–16903.
[17] N. Zhang, R. Ciriminna, M. Pagliaro, Y. Xu, Chem. Soc. Rev. 43 (2014) 5276–5287.
[18] W. Wang, W. Huang, Y. Ni, C. Lu, Z. Xu, ACS Appl. Mater. Inter. 6 (2013) 340–348.
[19] W. Fan, H. Bai, W. Shi, CrystEngComm 16 (2014) 3059.
[20] H. Li, R. Liu, Y. Liu, H. Huang, H. Yu, H. Ming, S. Lian, S.-T. Lee, Z. Kang, J. Mater. Chem. 22 (2012) 17470–17475.
[21] G. Wang, B. Huang, X. Ma, Z. Wang, X. Qin, X. Zhang, Y. Dai, M.H. Whangbo, Angew. Chem. 125 (2013) 4910–4913.
[22] Y. Lv, M. Yao, J.P. Holgado, T. Roth, A. Steiner, L. Gan, R.M. Lambert, D.S. Wright, RSC Adv. 3 (2013) 13659–13662.
[23] J. Tian, Y. Sang, G. Yu, H. Jiang, X. Mu, H. Liu, Adv. Mater. 25 (2013) 5075–5080.
[24] L. Bhira, H. Essaidi, S. Belgacem, G. Couturier, J. Salardenne, N. Barreaux, J. Bernede, Phys. Status Solidi A 181 (2000) 427–435.
[25] Y. He, D. Li, G. Xiao, W. Chen, Y. Chen, M. Sun, H. Huang, X. Fu, J. Phys. Chem. C 113 (2009) 5254–5262.
[26] X. Zhang, X. Li, C. Shao, J. Li, M. Zhang, P. Zhang, K. Wang, N. Lu, Y. Liu, J. Hazard. Mater. 260 (2013) 892–900.
[27] A.K. Nayak, S. Lee, Y. Sohn, D. Pradhan, CrystEngComm 16 (2014) 8064–8072.
[28] R. Jayakrishnan, T.T. John, C.S. Kartha, K. Vijayakumar, D. Jain, L.S. Chandra, V. Ganesan, J. Appl. Phys. 103 (2008) 053106.
[29] B. O'regan, M. Grfitzeli, Nature 353 (1991) 737–740.
[30] J. Shen, B. Yan, M. Shi, H. Ma, N. Li, M. Ye, J. Mater. Chem. 21 (2011) 3415–3421.
[31] L. Xiong, F. Yang, L. Yan, N. Yan, X. Yang, M. Qiu, Y. Yu, J. Phys. Chem. Solids 72 (2011) 1104–1109.
[32] X. Zhang, X. Li, C. Shao, J. Li, M. Zhang, P. Zhang, K. Wang, N. Lu, Y. Liu, J. Hazard. Mater. 260 (2013) 892–900.
[33] S. Rengaraj, S. Venkataraj, C.-W. Tai, Y. Kim, E. Repo, M. Sillanpää, Langmuir 27 (2011) 5534–5541.
[34] X. Fu, X. Wang, Z. Chen, Z. Zhang, Z. Li, D.Y.C. Leung, L. Wu, X. Fu, Appl. Catal. B: Environ. 95 (2010) 393–399.
[35] X. An, J.C. Yu, F. Wang, C. Li, Y. Li, Appl. Catal. B: Environ. 129 (2013) 80–88.
[36] D.C. Hurum, A.G. Agrios, K.A. Gray, T. Rajh, M.C. Thurnauer, J. Phys. Chem. B 107 (2003) 4545–4549.
[37] W. Zhou, G. Du, P. Hu, G. Li, D. Wang, H. Liu, J. Wang, R.I. Boughton, D. Liu, H. Jiang, J. Mater. Chem. 21 (2011) 7937–7945.
[38] B. Wozniak, J. Dera, Light Absorption in Sea Water, Springer, New York, 2007.
[39] W.Y. Wu, J.N. Schulman, T.-Y. Hsu, U. Efron, Appl. Phys. Lett. 51 (1987) 710–712.
[40] R. Jayakrishnan, T. Sebastian, T.T. John, C.S. Kartha, K.P. Vijayakumar, J. Appl. Phys. 102 (2007) 043109.
[41] D.F. Ollis, C.-Y. Hsiao, L. Budiman, C.-L. Lee, J. Catal. 88 (1984) 89–96.
[42] H. Al-Ekabi, N. Serpone, E. Pelizzetti, C. Minero, M.A. Fox, R.B. Draper, Langmuir 5 (1989) 250–255.
[43] K.-I. Ishibashi, A. Fujishima, T. Watanabe, K. Hashimoto, Electrochem. Commun. 2 (2000) 207–210.
[44] J.C. Barreto, G.S. Smith, N.H. Strobel, P.A. McQuillin, T.A. Miller, Life Sci. 56 (1994) PL89–PL96.